

Dynamic plasticity and failure of microscale glass: Rate-dependent ductile-brittle-ductile transition

Rajaprakash Ramachandramoorthy^{+1}, Jakob Schwiedrzik^{+1*}, Laszlo Petho¹, Carlos Guerra-
Nuñez¹, Damian Frey², Jean-Marc Breguet², Johann Michler^{1*}*

⁺ - Equal contribution

^{*} - Corresponding authors

¹ - Laboratory of Mechanics of Materials and Nanostructures,

Empa – Swiss Federal Laboratories for Materials Science and Technology,

Feuerwerkerstrasse 39,

3602 – Thun. Switzerland.

² - Alemnis AG,

Feuerwerkerstrasse 39,

3602 – Thun. Switzerland.

Keywords: High strain rate, amorphous, micromechanics, glass, plasticity

Abstract

Glass is recently envisioned as a stronger and more robust alternative to silicon in MEMS applications including high frequency resonators and switches. Identifying the dynamic mechanical properties of microscale glass is thus vital for understanding their ability to withstand shocks and vibrations in such demanding applications. But despite nearly half-a-century of research, the micromechanical properties of glass and amorphous materials in general, are

primarily limited to quasi-static strain rates below $\sim 0.1/s$. Here we report the *in situ* high strain rate experiments of fused silica micropillars inside a scanning electron microscope at strain rates up to 1335/s. A remarkable ductile-brittle-ductile failure mode transition was observed at increasing strain rates from 0.0008/s to 1335/s, as the deformation flow transitions between homogeneous-serrated-homogeneous regimes. Detailed surface topography investigation of the tested micropillars revealed that at the intermediate strain rate ($< \sim 6/s$) serrated flow regime, the load drops are caused by the sequential propagation of individual shear bands. Analytical calculations and FE simulations suggest that the atomistic mechanism responsible for the homogenous stress-strain curves at the very high strain rates ($> \sim 64/s$) can be attributed to the simultaneous nucleation of multiple shear bands along with dissipative deformation heating. This unique rate-dependent deformation behavior of the glass micropillars highlights the importance and need of extending such microscale high strain rate studies to other amorphous materials like metallic glasses and amorphous metals/alloys. Such investigations can provide critical insights about the damage tolerance and crashworthiness of these materials for real-life applications.

Main

Glass or fused silica is one of the oldest manmade materials dating back to 3500BC,¹ which is ubiquitous in several domestic, industrial, defense and scientific applications. Bulk glass, though strong, is inherently brittle and extremely sensitive to flaws, given its amorphous nature without any microstructural order. Recently, using advanced manufacturing techniques, three-dimensional (3D) micro-printing of fused silica glass has been made possible.² It is therefore seen now as an alternative to traditional silicon for fabricating complex microelectromechanical systems (MEMS) and microfluidic devices that are more robust, transparent and temperature resistant.^{3, 4} Given these MEMS based applications for fused silica and the size effects in brittle materials, their mechanical properties must be characterized at the microscale in order to

ascertain their reliability and robustness. Also, such MEMS devices are typically used in several high frequency applications such as accelerometers/resonators⁵ and they have to be robust enough to withstand shocks created from drop impacts.⁶ Such extreme applications require a clear understanding of the deformation mechanisms in microscale fused silica that operate at strain rates in excess of 1000/s. Unfortunately, till date the available mechanical properties of microscale fused silica are at quasi-static strain rates of $<\sim 0.02/\text{s}$.^{7, 8}

Amorphous materials such as fused silica do not have long range order, unlike their crystalline counterparts (quartz). The exact nature behind the deformation of such amorphous materials with short range order is still not clearly understood, but the fundamental unit process behind the deformation is the thermally activated local rearrangement of atoms that can accommodate shear strain. Two prominent mechanistic frameworks have been previously developed to explain such local arrangements in amorphous materials, namely, free-volume model by Spaepen⁹ and the STZ model by Argon.¹⁰ The free-volume model views the deformation as a series of discrete diffusive-like atomic jumps near sites of high free volume. On the other hand, the STZ model depicts the deformation as the combined effect of several shear events, where a few atoms collectively shuffle in shear under the influence of stress and temperature. It should be noted that the phenomenology of both models are essentially identical and the physical predications are also largely similar.¹¹ In this study, to explain the trends of deformation we will subscribe to the STZ model. In the STZ model, the amorphous materials deform via a three-step sequence. The first step involves the formation of the first STZ, a local rearrangement of a cluster of atoms, which can accommodate shear strain in the deformation volume (a thermally activated process) based on the transition state kinetic law.¹² The second step is the subsequent formation of secondary STZ's in the vicinity of initial STZ's that is influenced by their strain field and the free volume.¹³ These two steps keep repeating until a collection of multiple STZ's has been formed. This

collection of STZ's essentially form nucleation sites for shear bands, thin planar sections of material that can accommodate large shear strain during plastic deformation.¹⁴ In the third step of the deformation process, the shear band nucleus reaches a critical size and grows rapidly into a shear band. The applied strain rate in the bulk is partitioned onto the shear band, until the maximum velocity is reached. The fully developed shear band then begins to propagate by accumulating additional plastic deformation in the form of shear band slip.¹⁵

The main motivation for this study is to contribute towards enhancing the fundamental understanding of the physical properties of amorphous materials at high strain rates upto 1335/s. Amorphous materials, in general, possess better properties such as enhanced strength compared to their ordered crystalline counterparts. This is because in crystalline materials the atomic changes to create dislocations is a low energy process, while in amorphous materials, which lack long-range translational symmetry, it is a relatively high energy process.^{11, 16} The research on the micromechanical characterization of amorphous materials, so far, has been enabled by experimental testing at quasi-static strain rates^{7, 17} and by MD simulations primarily conducted at ultra-high strain rates ($\sim 10^6$ /s and higher) on metallic glasses.¹⁸ (For a brief literature survey of the rate-dependent mechanical studies in metallic glass, see Supplementary section S1). This mismatch in strain rates means that the experimental results cannot be compared directly to the results from MD simulations. Thus increasing the experimental strain rates in micromechanical testing is essential in bridging the gap between these two approaches.¹⁹

Also, there are several benefits for using miniaturized high speed testing systems including higher strain rates for a given actuation velocity due to smaller sample size, lower magnitude of inertial contributions and faster stress wave equilibration times. For example, the duration of an dynamic experiment conducted at 1000/s strain rate is $\sim 70\mu\text{s}$, both for macro- and microscale samples. Given that the elastic wave speed in fused silica is $\sim 5823\text{m/s}$,²⁰ the wave travel time in a

macroscale fused silica of 9mm thickness (typical thickness of sample used in Kolsky bar is 6-12mm)²¹ is $\sim 2\mu\text{s}$, while the wave travel time in a $5\mu\text{m}$ high fused silica micropillar is 1ns. Thus, in the macroscale, the time scale of experiment and the wave travel time is in the same order of magnitude, making the understanding of wave propagation phenomena vital. On the contrary, in the microscale the duration of the experiment far exceeds the wave travel time, essentially making the wave propagation phenomena irrelevant in these samples at strain rates less than $\sim 10^5/\text{s}$. This also means that the three reverberations of wave in the microscale specimen, generally accepted requirement for stress equilibration, are achieved within 3ns. Consequently, in dynamic micromechanical testing the elastic and plastic constitutive material properties of microscale samples can be obtained at very high strain rates, without interference from the elastic waves in the material. So intrinsically, exploring the high strain rate mechanical properties at the microscale is advantageous compared to their macroscale counterparts.

In this study, pristine fused silica micropillar arrays (>1000) were fabricated using lithography based technique (for more details refer to methodology section M1), hence avoiding the typical focused ion beam (FIB) induced damage due to Ga implantation²² in micropillars while tremendously decreasing the fabrication time.²³⁻²⁵ Subsequently, we present a systematic study on the compression testing of amorphous fused silica micropillars with a diameter of $\sim 1.4\mu\text{m}$ at strain rates ranging from 0.0008/s to 1335/s, a three orders of magnitude increase in strain rate compared to the state-of-the-art in micropillar compression. This high strain rate micropillar compression was enabled by a piezo based micromechanical tester capable of simultaneous high speed actuation and sensing (for more detailed information refer to methodology section M2). This allows for the first time to measure statistically relevant micromechanical properties of a quasi-brittle material such as fused silica at strain rates over six orders of magnitude.

Ductile-brittle-ductile failure mode transition

Macroscale fused silica is typically brittle,²¹ but it is known that at the microscale they exhibit significant ductility.^{8, 26} Similarly in this study, the fused silica micropillars compressed at quasi-static speeds, below strain rates of 0.01/s, exhibit a highly ductile plasticity behavior with smooth stress-strain relationships, as shown by the representative curves in Figure 1. At these very low strain rates of 0.0008/s and 0.008/s the micropillars kept deforming upto 65% strain without failure. At intermediate strain rates from 0.07/s to 6/s, the fused silica micropillars transition into a regime where the stress-strain behavior becomes serrated due to presence of stress drops, but in all these cases the micropillars were tested till complete failure, as shown in Figure 1. It can also be seen that the fused silica micropillars become almost purely brittle at 6/s strain rate.

When the strain rates are increased further beyond 64/s till 1335/s, fused silica micropillars exhibit pronounced plasticity again with very few stress drops before failure. The complete list of stress-strain curves is provided in the supplementary Figure S1. The authors acknowledge that the pillars used in this study have a taper of $\sim 6^\circ$. This taper is due to the etching of the protective aluminum layer itself used during the lithography process, which results in the increase of diameter with increasing height in the glass micropillars. It should also be noted that the taper in our micropillars lead to a localization of deformation on the top of the pillar. We also admit that the shear bands might interact with the local stress fields, which tend to be less uniaxial at the top of the pillar due to the friction between indenter and pillar. Furthermore, bending stresses can be induced at large deformation due to off-axis loading. Both these factors can have effects on the shear band kinetics. However, we want to stress that while the taper can induce such artifacts, the same is true for FIB damage and Ga implantation, which have been shown to influence the local microstructure at the pillar surface thus the mechanical behavior of the microspecimens.^{27, 28} The lithography process used in this study allowed us to perform many experiments on

microspecimens that were free of preparation-induced defects and thus represent well the behavior of the material.

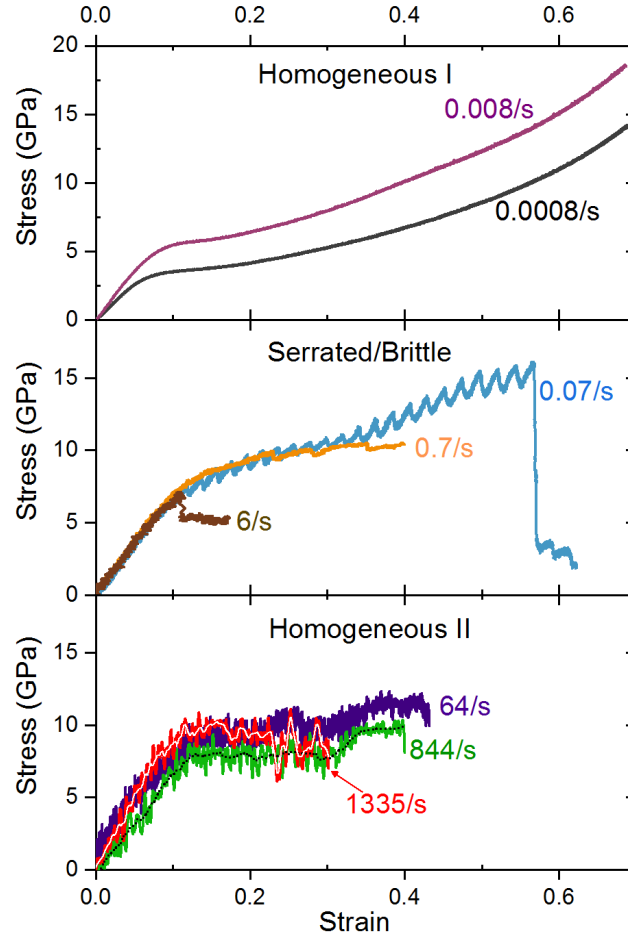


Figure 1: Rate-dependent representative stress-strain response of amorphous silica micropillars from 0.0008/s to 1335/s strain rate

Further, in order to understand the influence of taper on the absolute values such as loading modulus, yield stress, and hardening modulus, we conducted FEM simulations, the details of which can be found in the supplementary section S2. These correction factors were used to extract the correct material parameters from the experimental data (exhaustive list provided in supplementary table S1) and were henceforth used for all the analysis reported in this work. Also, the aspect ratio of all the silica micropillars is ~ 3.7 (height-to-diameter ratio). The critical elastic

buckling load for such micropillar geometry with $\sim 6^\circ$ taper is calculated as ~ 31 GPa,²⁹ which is significantly higher than the stresses achieved in the compression tests reported in this study. Also, the FEM analysis we conducted on the glass pillars did not show plastic buckling. Henceforth, the possibility of micropillar buckling has been neglected in this study. It should also be noted that though there is evidence that the mechanical properties of amorphous silica at the nanoscale is affected by intense electron beams such as from transmission electron microscopy (TEM), we did not observe any significant effects of the electron beam (see supplementary section S3).³⁰ Similar to the conclusions of the previous studies on the glass micropillars, we believe this can be attributed to the lower beam current density in the SEM and the larger sample sizes.⁸

Rate-dependent deformation kinetics in amorphous silica

Amorphous silica micropillars tested at quasi-static strain rates of 0.0008/s and 0.008/s exhibit a viscous flow or “Homogeneous I” flow, and this regime has already been thoroughly established in several previous works.^{11, 12, 31} During such slow strain rate experiments, the duration of the test (between 2mins and 15mins) is long enough for the STZ’s to form and the thermal fluctuations to distribute the STZ’s through the bulk of the amorphous silica micropillar.¹² As seen from Figure 1, the micropillars compressed at such quasi-static strain rates exhibit a smooth stress-strain relationship and high ductility (with only few cases showing one stress drop – Please see Supplementary Figure S1 for a comprehensive set of data), as the speed of internal structural reorganization is fast enough to accommodate the external loading rate.^{8, 32} Also, from a theoretical standpoint, using a micromechanical mean field model, it has been shown previously that at very low strain rates ($\sim 10^{-4}$ /s) the local weakening arising from the shear of a single STZ during deformation can be healed, before it can trigger an avalanche leading to the formation of a shear band.³¹

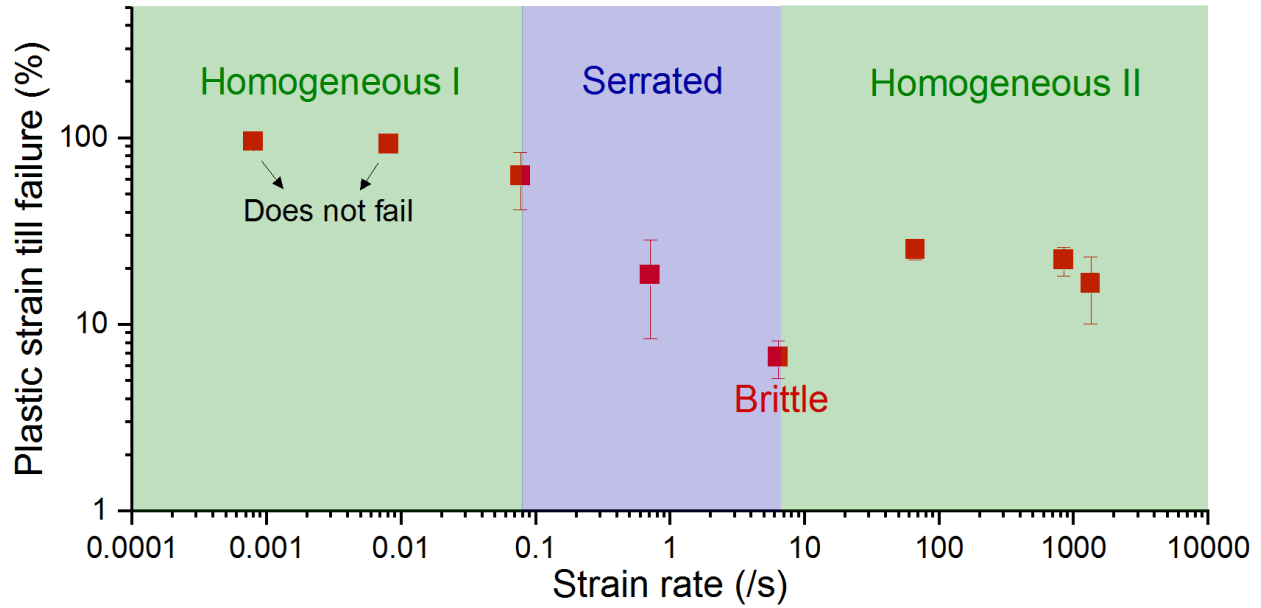


Figure 2: Plastic strain to failure in fused silica micropillars as a function of strain rates across six orders of magnitude

On the other hand, high strain rate compression tests on the amorphous silica pillars from 0.07/s till 1335/s, as seen from the stress-strain curves in Figure 1, led to unique ductile-serrated-brittle-ductile failure mode transition. This transition is again shown clearly in Figure 2, where the failure strain is plotted as function of strain rate. In order to interpret the mechanisms behind such remarkable rate-dependent phenomena in amorphous silica, a separate batch of fused silica micropillars were deformed up to a strain of 20% (before failure) at different strain rates. The pillars that were deformed till 20% strain at different strain rates were subsequently imaged using SEM to obtain the deformed shape and to capture potential rate-dependent surface features induced by deformation. The representative images of micropillars tested at four key strain rates at the serrated (from $\sim 0.07/s$ to $\sim 0.7/s$) and the homogeneous II (above $\sim 50/s$) flow regimes are shown in Figure 3 a)-d).

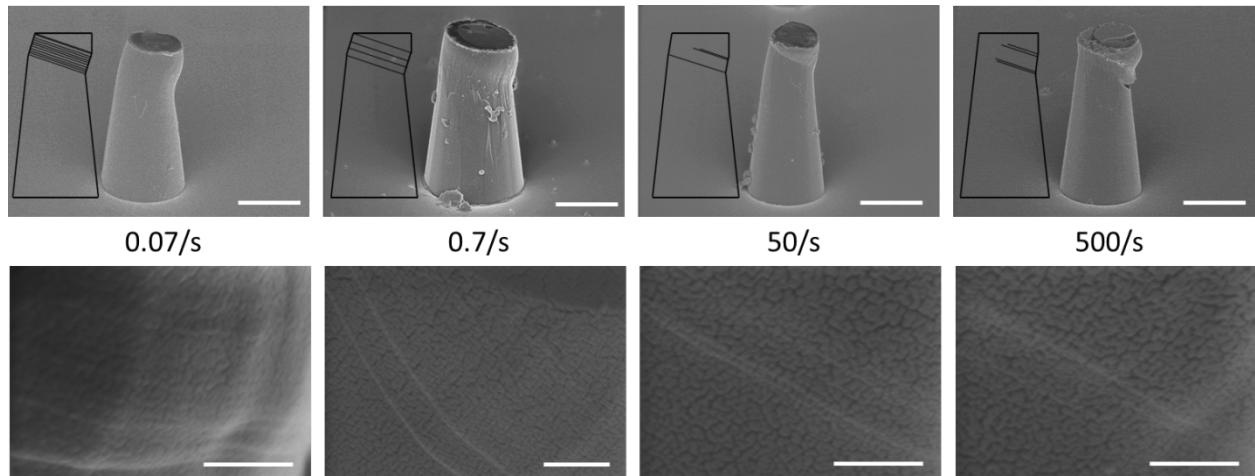


Figure 3a)-d): Amorphous silica micropillars strained till 20% at strain rates of 0.07/s, 0.7/s, 50/s and 500/s (Scale bar: 2μm). The surface of the micropillars tested at each strain rates are magnified to show the surface steps left by shear band propagation (Scale bar: 250 nm).

The Serrated flow regime in the silica micropillars is seen in the intermediate strain rates of $\sim 0.07/s$ to $\sim 6/s$, as depicted by the multiple stress drops in the respective stress-strain curves in Figure 1 and the extracted failure strains in Figure 2. A close investigation of the surface of the micropillars tested at these strain rates up to a total strain of 20%, as shown in Figure 3a) and b), reveals multiple shear band propagations that manifest as surface steps on the pillar. At the strain rate of 0.07/s, the most serrated flow profile is seen and this translates to the sequential formation of multiple individually propagated shear bands. Each of the stress drops in the stress-strain curve can be correlated to a propagated shear band induced surface step on the micropillar¹⁷ (the surface steps on the pillar were counted based on the intensity variations using an image processing software, Gatan Micrograph Suite). The same explanation can be applied for the case of 0.7/s strain rate where again the number of stress drops corresponds to the number of shear band. The only difference being at 0.7/s strain rate there are only three to four stress drops in the stress-strain curve and correspondingly only a few shear bands that have nucleated and propagated. It should also be noted that the spacing between the shear bands, where the shear

band slips and accumulates plasticity, increases when the strain rate was increased from 0.07/s to 0.7/s, as shown in the schematic in Figures 3a) and b). When the strain rate was further increased by one order of magnitude to ~ 6 /s, as the stress-strain curve shows in Figure 1, only one stress drop is seen and the micropillar fails in a brittle-like manner with very little plasticity. As such, the micropillar shatters completely during the test and any post-test analysis of the tested sample was not possible.

Further investigation of the loss of ductility with increase of strain rate from 0.07/s to 6/s was carried out by calculating the speed of stress drops from the experiments, which typically corresponds to the speed of the shear band propagation.³³ The ratio of the shear band propagation speed (mm/s) to the actuation speed (mm/s) used in the experiment at different strain rates in the Serrated regime has been plotted against the plastic strain in Figure 4. It can be clearly seen that when this ratio is kept low between one and five, significant plastic strain can be achieved in the silica micropillars, as a controlled progression of shear band nucleation, propagation and further slip on the shear band can be achieved. On the contrary, when the ratio is greater than five the silica micropillar cannot sustain a stable plasticity. In absolute terms, the average time taken for each stress-drop decreases from ~ 80 ms to ~ 0.5 ms, as the strain rate is increased from 0.07/s to 6/s. The average speed of the shear band propagation speed consequently increases by two orders of magnitude from ~ 0.002 mm/s to ~ 0.35 mm/s as the strain rate is increased by two orders of magnitude from 0.07/s (Please see Supplementary Table S2 for the comprehensive list of the extracted data, including the shear band displacement, time for strain burst and speed of the shear band propagation). We attribute this increase in shear band propagation speed with strain rate to the increased actuation speed at high strain rates, which overwhelms the shear band propagation speed.^{34, 35}

Interestingly, at even higher strain rates, from $\sim 64/\text{s}$ to $\sim 1335/\text{s}$, the silica micropillars enters another ductile failure regime or “Homogeneous II” regime, where a plastic strain of $\sim 20\%$ - 30% is reached, as shown in Figure 2. The stress-strain curves at these high strain rates, as seen in Figure 1, show that the micropillars fail in a homogeneous manner with a maximum of occasional one or two stress drops. Thus, the failure mode in silica micropillar transitions from a brittle to ductile regime with one order of increase in strain rate. A similar transition from inhomogeneous serrated flow at intermediate strain rates to homogeneous II flow regime at high strain rates above $1/\text{s}$ has been observed previously in metallic glasses using both rate-dependent nanoindentation and tension/compression experiments.^{12, 33, 36} The explanation for such a transition to Homogeneous II regime at high strain rates has been attributed to simultaneous nucleation of multiple shear bands.^{12, 33} At these very high strain rates above $\sim 64/\text{s}$, the plastic strain in the silica micropillars increase so quickly that the individual shear bands are not sufficient to accommodate the strain. Hence, the plastic strain is divided between multiple nucleated shear bands and only a few of them propagate fully, which again manifests as the few stress drops in the stress-strain response. This theory is further confirmed, by the high resolution images of the micropillar surface tested at these high strain rates shown in Figure 3c) and d). In both cases, at strain rate of $50/\text{s}$ and $500/\text{s}$, it can be seen that there are a few partially propagated shear bands (surface steps cover the circumference of the micropillar partially) and only few fully propagated shear bands (surface steps cover the entire pillar circumference), unlike the pillars in the inhomogeneous regime, seen in Figure 3a), where multiple fully propagated shear bands can be seen. It should be noted that homogeneous flow should not have any localized regions and the entire sample should undergo plastic deformation. But in few of the tests at high strain rates above $50/\text{s}$ strain rate, we do see one or two partial shear band propagations (as seen in Figure 3c), d)). This is also reflected in a few stress drops noticeable in some stress-strain curves at high

strain rates shown in Supplementary Figure S1. We believe the deformation mechanism behind the serrated (or) localized regime and the homogeneous II regime are predominantly controlled by shear band propagation and nucleation respectively, though in the homogeneous II regime occasional stochastic shear band propagations can occur. There are previous studies in the literature where similar distinctions between homogenous and highly localized flow have been established as a function of size and strain rate ($<3/s$) in metallic glasses.^{37, 38}

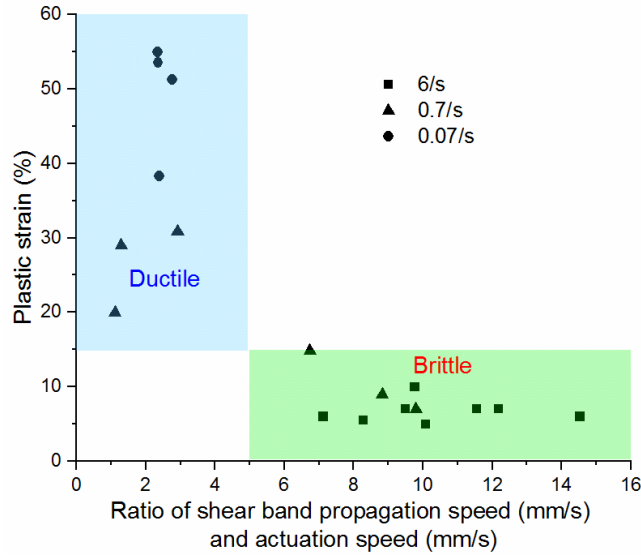


Figure 4: Dependence of the plastic strain on the ratio between the shear band propagation speed and the actuation speed across the three different strain rates in the Serrated regime.

Atomistic mechanisms behind the shear band kinetics

To further understand the atomistic mechanisms behind the ductile-serrated-brittle-ductile failure mode transition, we calculated the strain rate sensitivity ‘ m ’ using Equation 2 and the apparent activation volume ‘ V^* ’ at the point of yield, where it is assumed that the pillar microstructure is similar between tests conducted at different strain rates, using Equation 3 as used in previous studies.³⁹

$$m = \frac{d \ln \sigma}{d \ln \dot{\epsilon}} \quad (2)$$

$$V^* = k_B T \left(\frac{d \ln \dot{\epsilon}}{d \sigma} \right) \quad (3)$$

where k_B is the Boltzmann's constant, $\dot{\epsilon}$ is the strain rate and σ is the yield stress. These values are shown for the three different flow regimes in Figure 5, where the yield stress is plotted as a function of strain rate.

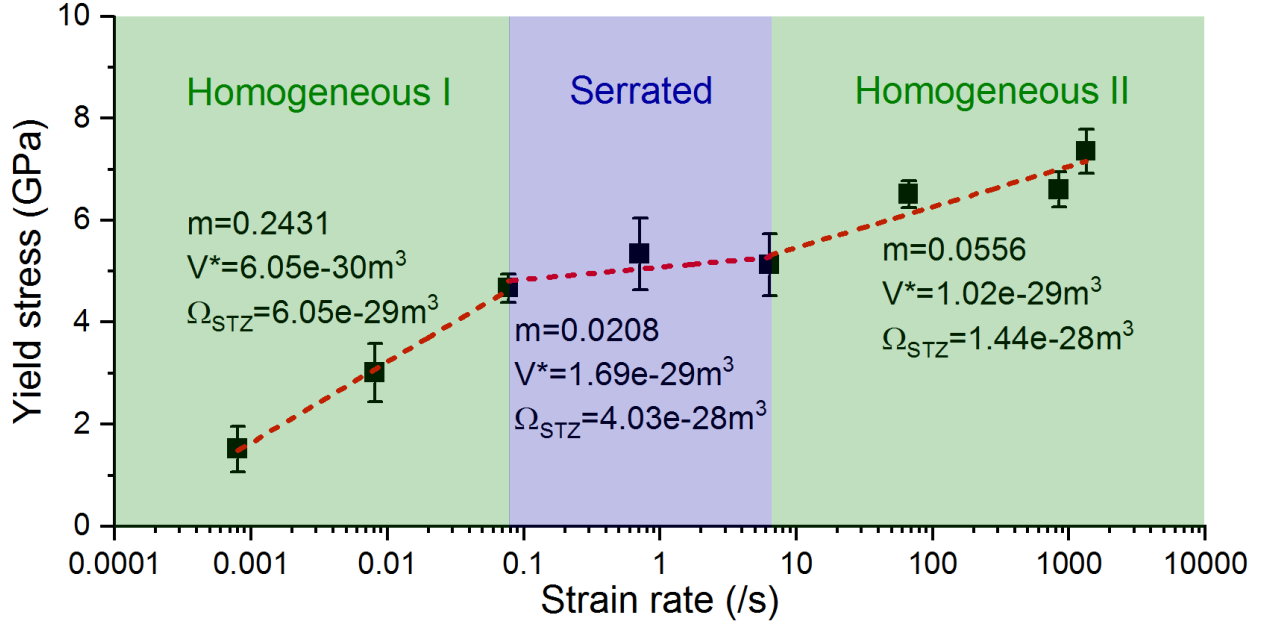


Figure 5: Yield stress at different flow regimes (corrected for taper), along with the key extracted data of strain rate sensitivity, apparent activation volume and STZ volume.

Amorphous silica has a high rate-sensitivity at low strain rates with a value of 0.2431. But as the system enters the Serrated regime the m value decreases by one order of magnitude to 0.0208 and subsequently at high strain rates in the Homogeneous II regime, the strain rate sensitivity again increases marginally to 0.0549. This shows that the yield stress of amorphous silica micropillars are strongly rate-dependent at strain rates below 0.07/s and at higher strain rates there is only a weak-dependence of the yield with strain rate. This change in rate-sensitivity at the three strain-rate regimes shows that there are three distinct deformation mechanisms in amorphous silica micropillars.⁴⁰ Also, since multiple micropillars were tested at each strain rate, a multivariate

regression study could be performed. This analysis showed that there is indeed a statistically significant dependence of the yield strength and plastic strain on the strain rate (please see Supplementary section S4). It should also be noted that at high strain rates of $\sim 1335/\text{s}$, a yield shear strength of $3.7 \pm 0.43 \text{ GPa}$ is obtained (angle of shear is approximated as 45°), which is close to the estimated ideal shear strength⁴¹ of fused silica, $G_0/2\pi = \sim 4.93 \text{ GPa}$ (where $G_0 = 31 \text{ GPa}$ is the estimated shear modulus of fused silica at 298 K).⁴²

Using the estimated apparent activation volumes shown in Figure 5 and the Johnson and Samwer's cooperative shearing model (CSM),⁴³ the STZ volume (Ω_{STZ}) and the apparent activation energy barrier (W^*) for the different regimes can be estimated using Equation 4 and Equation 5.^{39, 44}

$$\Omega_{STZ} = \frac{V^*}{6RG_0\gamma_c^2\xi\left(\frac{1}{\tau_c}\right)\left(1 - \frac{\tau}{\tau_c}\right)^{\frac{1}{2}}} \quad (4)$$

$$W^* = 4RG_0\gamma_c^2\xi\left(\frac{1}{\tau_c}\right)\left(1 - \frac{\tau}{\tau_c}\right)^{\frac{3}{2}}\Omega_{STZ} \quad (5)$$

where τ is the yield shear stress, τ_c is the ideal shear strength of fused silica, G_0 is the shear modulus of fused silica at 298 K , $\gamma_c = 0.1$ is the STZ strain and $R=1/4$ is the fold ratio, and $\xi=3$ is a correction factor arising from matrix confinement.^{39, 43} The average STZ volumes calculated for the three deformation regimes show that the STZ volume grows by approximately one order of magnitude between the Homogeneous I and Serrated regime and decreases from the Serrated to Homogeneous II regime. Consequently, using an average atomic radius (1.17 \AA) and atomic volume calculation (6.66 \AA^3) the number of SiO_2 groups in the STZ volume for the Homogeneous I, Serrated and Homogeneous II regimes were calculated as 9, 60 and 21 SiO_2 building blocks, which is similar to the values obtained for metallic glasses in previous studies.^{10, 12} Assuming the STZ's have a spherical profile, the diameter of the STZ's vary between 5, 9 and 7 SiO_2 building

blocks in the three flow regimes respectively, which is also consistent with previously reported values for amorphous materials.^{11, 12} Using the STZ volume, the apparent activation energy barriers for the three different regimes were obtained as 0.20 eV, 0.84eV and 0.19 eV, which is also in similar order of magnitude to metallic glasses.^{34, 45, 46} All the calculated values have been summarized in Table 1. It should be noted that we primarily use CSM as a tool to differentiate between the three different strain rate regimes rather than as an absolute measure. But it should be noted that in previous studies on metallic glasses using identical CSM parameters, similar values of the STZ's volumes and activation parameters have been obtained, though the chemical structures of metallic glasses and amorphous fused silica are entirely different.^{39, 47, 48} This shows that the deformation signatures responsible for the mechanical behavior across amorphous materials can indeed be similar. It should be noted that from a fundamental point of view the rate dependent deformation mechanisms that we observe in fused silica are due to the interplay between the experimental time scale and the inherent plastic transition rate of the groups of atoms (STZ's) in the amorphous material.

Table 1: Summary of extracted parameters from the stress-strain curves of amorphous silica in the different flow regimes.

Parameters	Homogenous I	Serrated	Homogenous II
Strain rate sensitivity 'm'	0.2431±0.057	0.0208±0.0133	0.0556±0.0099
Activation volume (m ³)	6.05E-30	1.69E-29	1.02E-29
Average STZ volume (m ³)	6.05E-29	4.03E-28	1.44E-28
Average STZ size (SiO ₂ building blocks)	9.09	60.52	21.63
Diameter of STZ (Å)	4.87	9.17	6.50
Average activation energy (eV)	0.20	0.84	0.19

The STZ volume and the apparent activation energy increases as the system transitions from Homogeneous I to Serrated regimes. The reason for such increase in apparent activation energy can be attributed to the reduction in time required for the influence of thermal fluctuations on the mechanical behavior at increasing strain rates from 0.0008/s to 6/s. The system thus transitions from a thermally activated to a progressively athermal regime. It can also be understood that in homogeneous I regime, the system can keep nucleating STZ's to accommodate the plastic strain while in the Serrated regime the system needs the nucleated STZ's to coalesce into shear band nuclei. This could be the reason for the lower apparent activation energy in homogeneous I regime compared to the Serrated regime, as the energy required for the cooperative movement of the nucleated STZ's to form the shear band nuclei requires higher apparent activation energy. Further, when the strain rate is increased beyond 6/s and the amorphous silica micropillars transition from Serrated to Homogeneous II regime, the STZ volume and the apparent activation energy again decreases. This combination along with the high stress levels, enable the simultaneous nucleation of multiple shear bands, more specifically the formation of shear band nuclei in the amorphous silica micropillars which accommodates the plastic strain. Previously, Harris et al conducted a study on metallic glasses using a modified kinetic Monte Carlo algorithm, to arrive at the same conclusion that the number of shear band nuclei increases with increasing strain rate.¹⁵ Due to the severely short duration of the tests at high strain rates only very few of the shear band nuclei reach the critical length and are able to propagate.^{12, 49} Thus, the ductility of amorphous silica micropillars at high strain rates can be attributed to their ability to partition the accumulated plastic strain to the simultaneously nucleated shear band nuclei.

Thermal influence on glass micropillar deformation

It has been hypothesized in previous studies on metallic glasses that there could be a local temperature increase in the shear band during the drop at fast enough shear band propagation.^{35,}

^{50, 51} Since it is difficult to measure the local temperature increase in the micropillar experimentally, we resorted to axisymmetric thermal finite element simulations, which also accounts for the conduction based heat dissipation to the bulk and the indenter tip (see methods section M3 for detailed methodology). As seen from Figure 6, it was found that a power-law relationship exists between the maximum temperature increase and the strain rate with an exponent of approximately 1.25.

Specifically, at 6/s strain rate, the temperature rise due to localized shear banding calculated by the thermal model was between 1 and 2.5K. While this is just an order of magnitude approximation, it seems to suggest that a temperature rise in the range of a few K can change the flow properties of fused silica micropillars quite substantially. We believe the local temperature increase in the shear band leads to an autocatalytic shear banding process that can aid in the apparent embrittlement of the material at 6/s strain rate.³⁴ Similarly in a previous study on metallic glasses, Klaumünzer et al showed that a temperature increase of 50°C increases the shear band propagation velocity by approximately one order magnitude.⁵¹ Thus, it is possible that the increase in temperature in the shear band with strain rate allows the stress drop to happen increasingly fast, from 0.002mm/s to 0.35mm/s as the strain rate is increased from 0.07/s to 6/s.¹¹

Also, we believe that the increase in pillar temperature helps in increasing the strain accommodated between the shear band propagations. The average displacement between shear band propagations increases from ~205nm to ~519nm as the strain rate is increased from 0.07/s to 0.7/s (Please see supplementary Figure S2 for a schematic of the process and Supplementary Table S2 for the comprehensive data on the displacement between shear band propagations). This can also be seen by the increased spacing between shear bands at 0.7/s in Figure 3b) compared to Figure 3a). Eventually, at a strain rate of ~6/s, the speed of stress drop is so high that the

micropillar cannot arrest the propagation of the first shear band; the micropillar slips at the first shear band and the pillar fails in a brittle-like manner.

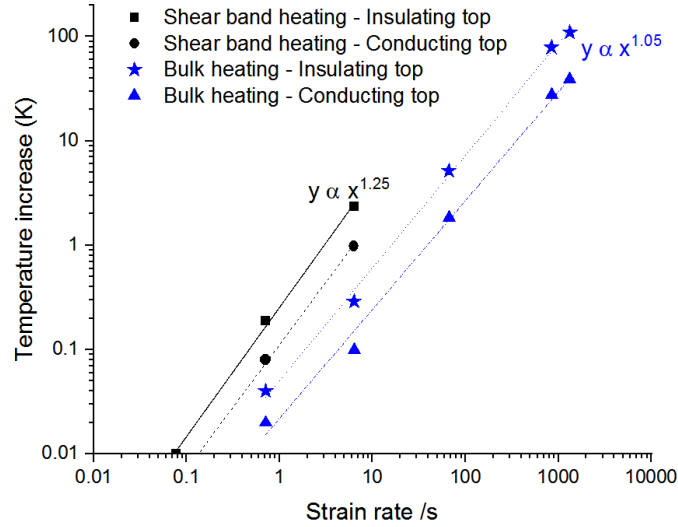


Figure 6: Finite elements based thermal modeling of shear band heating and bulk heating as a function of strain rate

Furthermore, at very high strain rates $>64/s$ there is a potential for temperature increase due to sudden dissipation of energy (1.1 GJ/m^3) in the whole micropillar, which could also aid in increasing the ductility of amorphous silica.¹² In order to determine the potential temperature increase in the micropillars due to bulk heating at these high strain rates, we again resorted to thermal FEM simulations of the fused silica micropillars at different strain rates (see methods section M3 for a detailed FEM methodology). We identified a power law based increase in temperature with strain rate, which has an exponent close to unity, as shown in Figure 6. While the temperature rise for low and intermediate strain rates up to $6/s$ were almost inexistent, starting at $64/s$ relevant temperature rises were seen of 2 to 5K depending on the boundary conditions. For the fastest experiments a temperature rise of even 40 to 110K was obtained. Thus, bulk heating starts to become relevant at higher strain rates and the flow behaviour in the whole pillar can be affected. Given that the shear band nucleation is a thermally activated process, bulk

heating could also aid in the nucleation of simultaneous shear bands in the pillar, leading to an apparent bulk deformation and an increase in apparent ductility at strain rates above 64/s.

However, it should be noted that we can only comment on correlations and not causality based on the experimental data and thermal simulations in this study. In other words, there could be other factors beyond just the temperature rise in the micropillars that could also affect the flow behavior.

In summary, fused silica micropillars exhibit strong rate-dependent mechanical properties, including yield strength and plastic strain. The deformation mechanisms behind such rate-dependent properties also vary significantly depending on the flow regime. As such in fused silica micropillars, at lower strain rates shear band propagation kinetics dictates the flow, while at higher strain rates shear band nucleation kinetics dominates, as individual shear band propagations cannot accommodate the applied strain quickly enough to relieve the high stress levels. It can be understood easily that similar high strain rate micromechanical investigations of other amorphous materials such as bulk metallic glasses, amorphous glassy carbon etc., can provide unique insights into their deformation behavior at extreme but application-relevant conditions. Future work on the dynamic compression of other amorphous materials can shed light into whether such transitions in deformation behavior at different strain rates are universal or specific to specific amorphous materials and can have profound implications on their suitability in different applications to withstand impacts and drops. Also, as mentioned before, high strain rate micromechanical experiments help in bridging time-scales between experiments and simulations, which can lead to the accelerated design and discovery of functional amorphous materials with tunable physical properties.⁵²

Methods

M1. Lithography based fabrication of fused silica micropillars

The fused silica micropillars were fabricated using a traditional deposition, mask and etch lithography technique. Hence these micropillars have pristine surfaces, unlike the traditional FIB made pillars that typically have a damage layer due to the Ga implantation. Also, due to the large milling time for FIB made pillars, the number of test samples in micromechanical tests are typically kept low. On the contrary, given that the pillars used in this study are lithography made, a large number of pillars (>1000) can be produced on the same glass substrate and the pillars are perfectly reproducible, as shown in Figure 7.

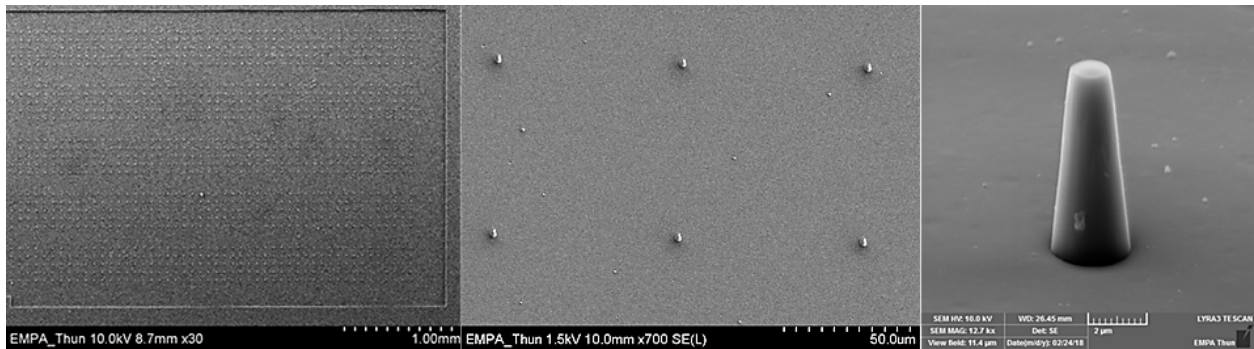


Figure 7: Array of fused silica micropillars fabricated using lithography magnified progressively. For the microfabrication of the $\sim 1.4\mu\text{m}$ diameter fused silica micropillars, fused silica wafers of $500\mu\text{m}$ thick and 100mm diameter were used as substrates. The low selectivity between the photoresist and glass during the etch process requires the use of a hard mask. For this purpose, a 300nm thick aluminum layer was magnetron sputtered onto the substrate using an Alliance-Concept DP650 sputter system. To pattern the hard mask, the substrate was spin coated with a $2\mu\text{m}$ thick positive tone photoresist layer (AZ 1512, Microchemicals GmbH). The layout was defined using a Heidelberg MLA150 direct laser writer, by a 405nm laser light source, $102\text{mJ}/\text{cm}^2$ dose and $1\mu\text{m}$ beam diameter. The exposed pattern was cleared by immersion into a developer solution (AZ 726 MIF, Microchemicals GmbH). The hard mask was dry etched in a

STS Multiplex ICP plasma system. A mixture of Cl_2 and BCl_3 gases resulted in a 350nm/min etch rate. Finally, the layout was transferred into the substrate by dry etching in a SPTS APS plasma etcher. A combination of C_4F_8 and O_2 gases etched the fused silica with a rate of 750nm/min. To facilitate the removal of the aluminum mask, the wafer was placed into a Tepla Gigabatch stripper for 10mins; where the oxygen plasma cleans the surface from etch residues. Then, the mask was removed by immersion into a commercial aluminum etchant (ANPE, Microchemicals GmbH) and the substrate was rinsed in deionized water. The wafer was recoated with a 14 μm thick protective photoresist layer (AZ9260, Microchemicals GmbH), to safeguard the pillars during the dicing step. For this purpose, a Disco DAD321 automated wafer dicing saw was used to slice the substrate into 10x10mm squares. The protective coating was finally removed by rinsing the chip in acetone and isopropanol.

M2. High strain rate micromechanical testing

The Alemnis high dynamic *in situ* nanoindenter used in this study has a piezoelectric actuator that is powered using a high voltage high speed amplifier capable of inputting high voltages (upto $\pm 175\text{V}$) across a variety of time scales, with very high slew rates ($\sim 350\text{V}/\mu\text{s}$). This allows the piezoelectric actuator to move with a speed up to $\sim 3\text{mm/s}$. The strain gages that are embedded in the piezoelectric actuator are capable of capturing these high speed displacements with a resolution of $\sim 15\text{nm}$.⁵³ The displacement voltage signals are acquired using a data acquisition board capable of high speed sampling up to 50k samples/s. The load cell used in this study is also a piezoelectric transducer that will output a charge in response to a change in force and in this high strain rate testing setup the diamond flat punch is mounted on the piezoelectric load cell as shown in Figure 8. The piezoelectric load cell can sense changes in load at high frequencies up to 10kHz, with a resolution of 30 μN . The load signals at strain rates less than 6/s are captured using a data acquisition system, again with high speed acquisition capability up to 50k samples/s. But

for tests conducted at even higher strain rates of 64/s and beyond, the amplified load signal from the charge amplifier is captured using an oscilloscope in order to acquire a non-aliased signal, using its ultra-high sampling rates of $\sim 2.5\text{G}$ samples/s. The load and the displacement signals are then time synchronized using a custom built code, in order to obtain a proper load-displacement curve. The load-displacement curves are later converted to a stress-strain curve, using the top cross-sectional area of the pillar and the height of the pillar respectively. Given that the majority of the deformation is focused on top $1/3^{\text{rd}}$ of the pillar, even at very high strains, the assumption of using the pillar's top cross-section to obtain the stress remains valid. The quasi-static compression tests conducted at strain rates below 0.7/s were conducted using piezoelectric actuation at slow speeds and a strain gage based load cell, the details of which are mentioned in detailed elsewhere.⁵³ Another advantage of using the high stiffness piezoelectric actuator and piezoelectric load cell in combination with a stiff frame is that the combined machine compliance is reduced to a very low value of $\sim 6.2\text{e-}7\text{m/N}$. This means that the high strain rate tests are essentially conducted at intrinsic displacement control. By varying the input voltage amplitude to the piezoelectric actuator, a pre-defined displacement profile (or velocity profile), or consequently a precise strain can be induced in the micropillar. This means the high strain rate tests can be stopped at a pre-defined strain and the sample can be recovered properly. The recovered sample can then be post-processed to obtain vital information about the deformation mechanisms by further detailed investigation under a scanning electron microscope (SEM) or transmission electron microscope (TEM) as necessary, as shown in Figure 3, for the silica pillars used in this study.

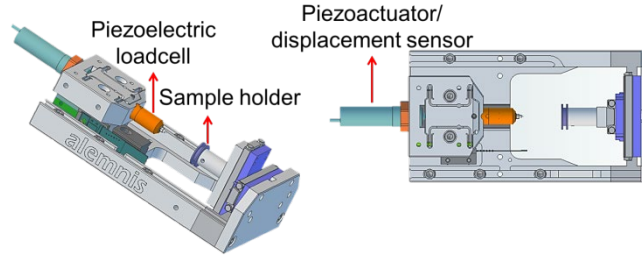


Figure 8: Schematic of the Alemnis high strain rate nanoindenter

M3. FEM methodology

Axisymmetric thermal finite element simulations were performed using Comsol Multiphysics 5.3. The tapered pillar was modeled as standing on a substrate with $10\mu\text{m}$ radius and height. The boundaries of the simulated substrate to the infinite half space were modeled as constant temperature boundaries. It was assumed and verified that they are sufficiently far away from the pillar not to affect the local solution in the pillar. 2889 triangular domain elements and 171 boundary elements were defined. The boundaries exposed to vacuum in the experiment were modeled as isolated boundaries, effects of radiative heat loss were not considered. For the boundary at the top of the pillar in contact with the indenter tip, two extreme cases were considered: Isolated boundary for the case when there is a high interfacial thermal resistance and constant temperature boundary if it is assumed that the indenter tip acts as a heat sink and the interfacial thermal resistance is very low. Two different heat sources were considered depending on the observed deformation mechanism: For strain rates between $0.07/\text{s}$ and $6/\text{s}$, local heating in a shear band during a load drop was assessed. For this, the average stress drop, the ultimate stress before the drop, and the duration of the drop were determined from the experimental data.

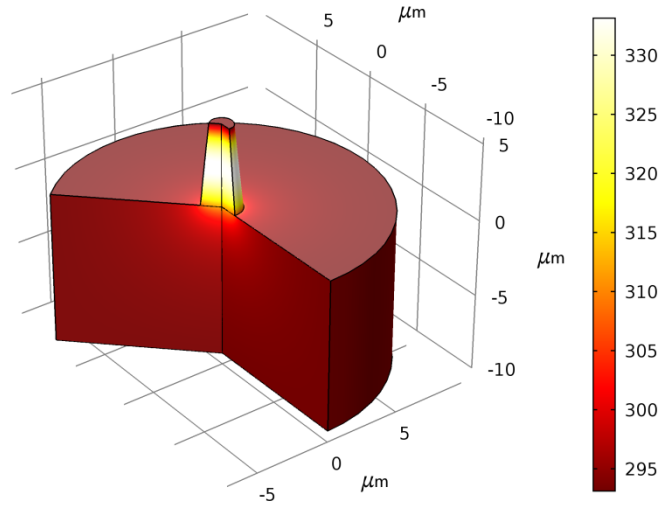


Figure 9: Example of a COMSOL thermal simulation conducted to understand the temperature rise in the glass pillars at high strain rates

Assuming constant modulus, the axial strain burst was calculated and converted to a shear strain burst by assuming that the complete axial deformation burst is localized in a single shear band oriented at 45° to the loading axis with an average thickness of 15nm. The power density dissipated in the shear band was then calculated by integrating the shear stress - shear strain curve during the drop event and dividing by the duration of the drop. Then an artificial boundary was introduced at 2/3 of the pillar height mimicking a single shear band and the calculated dissipated power density multiplied by the assumed shear band thickness was introduced using a boundary heat source. Thermal simulations were then run for the experimentally determined duration of the stress drop event and the maximum change in temperature was calculated. For all experimental strain rates, also volumetric heating of the pillar due to bulk plastic deformation was considered. For this purpose, the plastic energy density was determined for each experiment by integrating the area under the stress-strain curve and subtracting the elastic contribution. This energy density was subsequently converted to a power density by dividing it by the total duration of the experiment. This power density was then introduced into the whole pillar as a body heat source.

Thermal simulations were run for the full duration of the experiment and the maximum temperature rise in the pillar was calculated and a representative temperature map in the pillar is shown in Figure 9.

Furthermore, 3D mechanical finite element simulations were performed to ascertain the impact of taper on the mechanical properties using the commercial implicit solver Abaqus/Standard. The tapered pillar ($d_{\text{top}} = 1.46\mu\text{m}$, $d_{\text{bot}} = 2.5\mu\text{m}$, height = $5.41\mu\text{m}$) was placed on a substrate material with $5\mu\text{m}$ thickness and $5\mu\text{m}$ radius to account for substrate compliance. The boundaries of the substrate were fixed in all directions. The flat punch indenter was modeled as a rigid solid in contact with the top of the pillar. Hard contact and a friction coefficient of 0.1 were chosen for the interaction parameters in line with literature.⁵⁴ An elastic modulus of 70GPa and a Poisson ratio of 0.18 were used. Following the suggestions of Kermouche and Bruns,^{8, 55} the plastic deformation of fused silica was modeled using the cap plasticity model with a uniaxial yield stress of 7.5GPa, a cap stress of 11.5GPa, a friction angle of $1\text{e-}4^\circ$, the transition parameter a of 1, an isotropic shape in the deviatoric plane ($K=1$), and no initial volumetric plastic strain. Cap hardening was defined with a volumetric plastic hardening slope of 100GPa. This plasticity model resembles a von Mises criterion with a yield stress of 7.5GPa and a cap allowing volumetric plastic deformation in compression. The pillar and substrate were meshed with approximately 8000 linear hexahedral elements (C3D8) and compressed by $1.2\mu\text{m}$ in displacement control. Force was converted to engineering stress by dividing the load data by the initial top area of the tapered pillar. Displacement was corrected for substrate compliance using the modified Sneddon approach⁵⁶ and the bottom diameter of the pillar and converted to engineering strains by dividing the corrected displacement by the initial height of the pillar. Yield stress was determined by assuming bilinear material behavior and finding the intersection of two lines fitted to the initial elastic and the hardening part of the simulated stress strain curve.

Plastic strain was computed by subtracting the elastic from the total strain, i.e. using $\varepsilon_{pl} = \varepsilon - \frac{\sigma}{E_{app}}$ with the apparent modulus determined by fitting the elastic loading part of the stress-strain curve with a straight line. Hardening slope was determined by fitting a line to the post-yield stress as a function of plastic strain.

ASSOCIATED CONTENT

Supporting Information

The supporting information file contains the following information:

- i) Section S1: Literature survey rate-dependent amorphous metallic glass testing
- ii) Figure S1: Comprehensive stress-strain curves obtained at different strain rates
- iii) Figure S2: Schematic of the sequential shear band propagations
- iv) Table S1: Extracted parameters from stress-strain curves at different strain rates
- v) Table S2: Shear band propagation speed for the different experiments in the serrated strain rate regime
- vi) Section S2: FEM modeling to correct for taper
- vii) Section S3: Effects of electron beam radiation
- viii) Section S4: Statistical Analysis

The following files are available free of charge

HSR Glass - Supporting Information.pdf

AUTHOR INFORMATION

Corresponding Authors

Rajaprakash Ramachandramoorthy, Jakob Schwiedrzik and Johann Michler.

Laboratory of Mechanics of Materials and Nanostructures,

Empa – Swiss Federal Laboratories for Materials Science and Technology,

Feuerwerkerstrasse 39,

3602 – Thun. Switzerland.

Email: rajaprakash.ramachandramoorthy@empa.ch, jakob.schwiedrzik@empa.ch,

johann.michler@empa.ch

Author Contributions

The initial planning of the project was done by R.R., J.S., J.M.B and J.M. The glass micropillars were fabricated by L.P. The high strain rate *in situ* micropillar compression experiments were conducted by R.R, with the technical assistance of D.F. The FEM simulations on the micropillars were conducted by J.S. The RAMAN data was collected by C.G.N along with the help of R.R. Data analysis was performed by R.R. and J.S. with the assistance of D.F and interpreted with the help of J.M.B. and J.M. The manuscript was written by R.R. and J.S. with contributions from all the authors.

Funding Sources

The authors would like to acknowledge funding by the Horizon 2020 Marie Skłodowska-Curie Action (MSCA) COFUND program EMPAPOSTDOCS, the Swiss Commission for Technology and Innovation (CTI) project FASTOBS (grant no. 18003.1 PFNM-NM), and the Swiss National Science Foundation (SNSF) Ambizione grant no. 174192.

ACKNOWLEDGEMENT

The authors thank Mr. Patrick Schürch for the 3D rendering of graphical abstract. Also, we would like to acknowledge Prof. Christopher Schuh for his valuable discussions on amorphous plasticity.

Conflict of Interest Disclosure

The authors declare no conflict of interest.

REFERENCES

1. Le Bourhis, E., *Glass: mechanics and technology*. John Wiley & Sons: 2014.
2. Kotz, F.; Arnold, K.; Bauer, W.; Schild, D.; Keller, N.; Sachsenheimer, K.; Nargang, T. M.; Richter, C.; Helmer, D.; Rapp, B. E. *Nature* **2017**, 544, 337.
3. Lenssen, B.; Bellouard, Y. *Applied Physics Letters* **2012**, 101, 103503.
4. Schaap, A.; Bellouard, Y.; Rohrlack, T. *Biomedical optics express* **2011**, 2, 658-664.
5. Acar, C.; Shkel, A. M. *Journal of Micromechanics and Microengineering* **2003**, 13, 634.
6. Mariani, S.; Ghisi, A.; Corigliano, A.; Zerbini, S. *Sensors* **2007**, 7, 1817-1833.
7. Lacroix, R.; Kermouche, G.; Teisseire, J.; Barthel, E. *Acta Materialia* **2012**, 60, 5555-5566.
8. Kermouche, G.; Guillonnet, G.; Michler, J.; Teisseire, J.; Barthel, E. *Acta Materialia* **2016**, 114, 146-153.
9. Spaepen, F. *Acta metallurgica* **1977**, 25, 407-415.
10. Argon, A. *Acta metallurgica* **1979**, 27, 47-58.
11. Schuh, C. A.; Hufnagel, T. C.; Ramamurty, U. *Acta Materialia* **2007**, 55, 4067-4109.
12. Schuh, C. A.; Lund, A. C.; Nieh, T. *Acta Materialia* **2004**, 52, 5879-5891.
13. Homer, E. R.; Schuh, C. A. *Acta Materialia* **2009**, 57, 2823-2833.
14. Liu, Y. H.; Wang, G.; Wang, R. J.; Pan, M. X.; Wang, W. H. *science* **2007**, 315, 1385-1388.
15. Harris, M. B.; Watts, L. S.; Homer, E. R. *Acta Materialia* **2016**, 111, 273-282.
16. Packard, C.; Franke, O.; Homer, E.; Schuh, C. *Journal of Materials Research* **2010**, 25, 2251-2263.
17. Dubach, A.; Raghavan, R.; Löffler, J. F.; Michler, J.; Ramamurty, U. *Scripta Materialia* **2009**, 60, 567-570.
18. Cao, A.; Cheng, Y.; Ma, E. *Acta Materialia* **2009**, 57, 5146-5155.
19. Ramachandramoorthy, R.; Milan, M.; Lin, Z.; Trolier-McKinstry, S.; Corigliano, A.; Espinosa, H. *Extreme Mechanics Letters* **2018**.
20. Strassburger, E.; Patel, P.; McCauley, J.; Templeton, D. In *High-Speed Photographic Study of Wave Propagation and Impact Damage in Fused Silica and ALON Using the Edge-On Impact (EOI) Method*, AIP Conference Proceedings, 2006; AIP: pp 892-895.
21. Daryadel, S. S.; Mantena, P. R.; Kim, K.; Stoddard, D.; Rajendran, A. *Journal of Non-Crystalline Solids* **2016**, 432, 432-439.
22. Lauener, C.; Petho, L.; Chen, M.; Xiao, Y.; Michler, J.; Wheeler, J. M. *Materials & Design* **2018**, 142, 340-349.
23. Jennings, A. T.; Li, J.; Greer, J. R. *Acta Materialia* **2011**, 59, 5627-5637.
24. Mohanty, G.; Wheeler, J. M.; Raghavan, R.; Wehrs, J.; Hasegawa, M.; Mischler, S.; Philippe, L.; Michler, J. *Philosophical Magazine* **2015**, 95, 1878-1895.
25. Dimiduk, D. M.; Woodward, C.; LeSar, R.; Uchic, M. D. *Science* **2006**, 312, 1188-1190.
26. Marsh, D. *Proc. R. Soc. Lond. A* **1964**, 279, 420-435.
27. Mačković, M.; Przybilla, T.; Dieker, C.; Herre, P.; Romeis, S.; Stara, H.; Schrenker, N.; Peukert, W.; Spiecker, E. *Frontiers in Materials* **2017**, 4, 10.
28. El-Awady, J. A.; Woodward, C.; Dimiduk, D. M.; Ghoniem, N. M. *Physical Review B* **2009**, 80, 104104.
29. Yossif, W. V. *Journal of Engineering and Sustainable Development* **2008**, 12, 148-160.
30. Mačković, M.; Niekiet, F.; Wondraczek, L.; Spiecker, E. *Acta Materialia* **2014**, 79, 363-373.

31. Cao, P.; Dahmen, K. A.; Kushima, A.; Wright, W. J.; Park, H. S.; Short, M. P.; Yip, S. *Journal of the Mechanics and Physics of Solids* **2018**, 114, 158-171.
32. Lu, J.; Ravichandran, G.; Johnson, W. L. *Acta materialia* **2003**, 51, 3429-3443.
33. Yang, B.; Nieh, T. *Acta Materialia* **2007**, 55, 295-300.
34. Klaumünzer, D.; Maaß, R.; Torre, F. H. D.; Löffler, J. F. *Applied Physics Letters* **2010**, 96, 061901.
35. Maaß, R.; Klaumünzer, D.; Löffler, J. F. *Acta Materialia* **2011**, 59, 3205-3213.
36. Sergueeva, A.; Mara, N.; Kuntz, J.; Lavernia, E.; Mukherjee*, A. *Philosophical Magazine* **2005**, 85, 2671-2687.
37. Tönnies, D.; Maaß, R.; Volkert, C. A. *Advanced Materials* **2014**, 26, 5715-5721.
38. Jang, D.; Gross, C. T.; Greer, J. R. *International Journal of Plasticity* **2011**, 27, 858-867.
39. Pan, D.; Inoue, A.; Sakurai, T.; Chen, M. *Proceedings of the National Academy of Sciences* **2008**, 105, 14769-14772.
40. Dubach, A.; Dalla Torre, F. H.; Löffler, J. F. *Acta Materialia* **2009**, 57, 881-892.
41. Bei, H.; George, E. P.; Hay, J.; Pharr, G. M. *Physical review letters* **2005**, 95, 045501.
42. DOREMUS, R. H. *Journal of the American Ceramic Society* **1966**, 49, 461-462.
43. Johnson, W.; Samwer, K. *Physical review letters* **2005**, 95, 195501.
44. Wang, N.; Ding, J.; Yan, F.; Asta, M.; Ritchie, R. O.; Li, L. *npj Computational Materials* **2018**, 4, 19.
45. Greer, A.; Cheng, Y.; Ma, E. *Materials Science and Engineering: R: Reports* **2013**, 74, 71-132.
46. Rodney, D.; Schuh, C. A. *Physical Review B* **2009**, 80, 184203.
47. Cheng, Y.; Ma, E. *Acta Materialia* **2011**, 59, 1800-1807.
48. Pauly, S.; Gorantla, S.; Wang, G.; Kühn, U.; Eckert, J. *Nature materials* **2010**, 9, 473.
49. Wang, L.; Lu, Z.; Nieh, T. *Scripta Materialia* **2011**, 65, 759-762.
50. Cheng, Y.; Han, Z.; Li, Y.; Ma, E. *Physical Review B* **2009**, 80, 134115.
51. Klaumünzer, D.; Maaß, R.; Löffler, J. F. *Journal of materials research* **2011**, 26, 1453-1463.
52. Jain, A.; Ong, S. P.; Hautier, G.; Chen, W.; Richards, W. D.; Dacek, S.; Cholia, S.; Gunter, D.; Skinner, D.; Ceder, G. *Apl Materials* **2013**, 1, 011002.
53. Guillonneau, G.; Mieszala, M.; Wehrs, J.; Schwiedrzik, J.; Grop, S.; Frey, D.; Philippe, L.; Breguet, J.-M.; Michler, J.; Wheeler, J. M. *Materials & Design* **2018**, 148, 39-48.
54. Yurkov, A.; Skvortsov, V.; Buyanovsky, I.; Matvievsky, R. *Journal of materials science letters* **1997**, 16, 1370-1374.
55. Bruns, S.; Johanns, K. E.; Rehman, H. U.; Pharr, G. M.; Durst, K. *Journal of the American Ceramic Society* **2017**, 100, 1928-1940.
56. Zhang, H.; Schuster, B. E.; Wei, Q.; Ramesh, K. T. *Scripta Materialia* **2006**, 54, 181-186.